Fuel 358 (2024) 130203

Contents lists available at ScienceDirect

Fuel

journal homepage: www.elsevier.com/locate/fuel

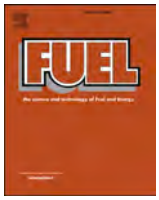

Full Length Article

Synergistic dual-regulating the electronic structure of NiMo selenides composite for highly efficient hydrogen evolution reaction

Rong Li [a,1], Song Xie [a,1], Yujie Zeng [a], Qiangqiang Zhao [a], Minqin Mao [a], Zhitian Liu [a], Paul K. Chu [b], Xiang Peng [a,*]

[a] Hubei Key Laboratory of Plasma Chemistry and Advanced Materials, Engineering Research Center of Phosphorus Resources Development and Utilization of Ministry of Education, School of Materials Science and Engineering, Wuhan Institute of Technology, Wuhan 430205, China

[b] Department of Physics, Department of Materials Science and Engineering, and Department of Biomedical Engineering, City University of Hong Kong, Tat Chee Avenue, Kowloon, Hong Kong, China

ARTICLE INFO

Keywords:
Hydrogen evolution reaction
Synergistic effect
NiMo selenides composite
Electronic structure modulation
Oxidation state tuning

ABSTRACT

Large-scale hydrogen production *via* electrochemical water splitting is important to renewable energy generation and the global drive toward low carbon emission. However, because of the sluggish kinetics and high energy consumption, efficient and economical electrocatalysts are required for the hydrogen evolution reaction (HER) in order to make it commercially viable. Herein, we present a dual-regulation strategy to optimize the electronic structure of NiMo selenides (NMS) composite for HER. By capitalizing on the electronic interactions between Ni and Mo atoms through the *in situ* phase separation of $Ni_{0.85}Se$ and $MoSe_2$ from $NiMoO_4$, the electronic configuration is optimized. The selective reduction is simultaneously performed to tune the oxidation states of Ni and Mo, which is more favorable for the adsorption of water molecules and desorption of hydrogen. The NMS electrocatalyst shows an overpotential of 124 mV for a current density of 10 mA cm^{-2}, a small Tafel slope of 63 mV dec^{-1} in alkaline electrolytes, Faradaic efficiency of 98.9 % in hydrogen production, as well as excellent long-term stability for 170 h. The results reveal a valuable strategy of synergistic dual-regulating the electronic structure of the active sites to design and prepare inexpensive and high-performance electrocatalysts for alkaline HER and related applications.

1. Introduction

Hydrogen is a clean and sustainable fuel that has the potential to replace traditional fossil fuels in the global effort to reduce the carbon footprint and combat climate change. The production of hydrogen through the hydrogen evolution reaction (HER) in water electrolysis represents a convenient and environmentally friendly technique [1,2]. However, HER suffers from sluggish kinetics and high overpotentials [3,4]. Pt-group metals are the benchmark electrocatalysts for HER, while their natural scarcity and high cost have hampered wide industrial implementation [5–7]. Therefore, more economical and readily available transition metal oxides [8,9], hydroxides [10], sulfides [11,12], phosphides [13], carbides [14], selenides [15], and nitrides [16] have been proposed as alternatives.

Two-dimensional layered molybdenum chalcogenides are promising electrocatalysts for HER due to their favorable hydrogen adsorption-free energy (ΔG_H) and tunable active center [17,18]. However, owing to the large number of inert basal sites on the surface [19], heterostructure engineering has emerged as a rational strategy to optimize the electronic structure of the surface sites to promote HER activity [20,21]. For instance, Tian et al. have prepared a three-dimensional $MoSe_2$@$Ni_{0.85}Se$ nanowire network for alkaline HER [22], Zhang et al. have anchored 1*T*-$MoSe_2$ nanosheets on NiSe nanowires to produce the 1*T*-$MoSe_2$/NiSe heterostructure with attractive electrocatalytic properties [23], and Ren et al. have prepared a heterostructure consisting of molybdenum sulfoselenide particles on nickel selenide foam which only requires an overpotential of −69 mV for a current density of 10 mA cm^{-2} with a small Tafel slope of 42.1 mV dec^{-1} for acidic HER by taking advantage of the interactions between the Ni- and Mo-based components in the heterostructure [24].

In addition to the interactions between Ni and Mo to activate the inert sites on the surface, the oxidation state of these atoms plays a

* Corresponding author.
E-mail address: xpeng@wit.edu.cn (X. Peng).
[1] These authors contributed equally to this work.

https://doi.org/10.1016/j.fuel.2023.130203
Received 30 August 2023; Received in revised form 23 October 2023; Accepted 26 October 2023

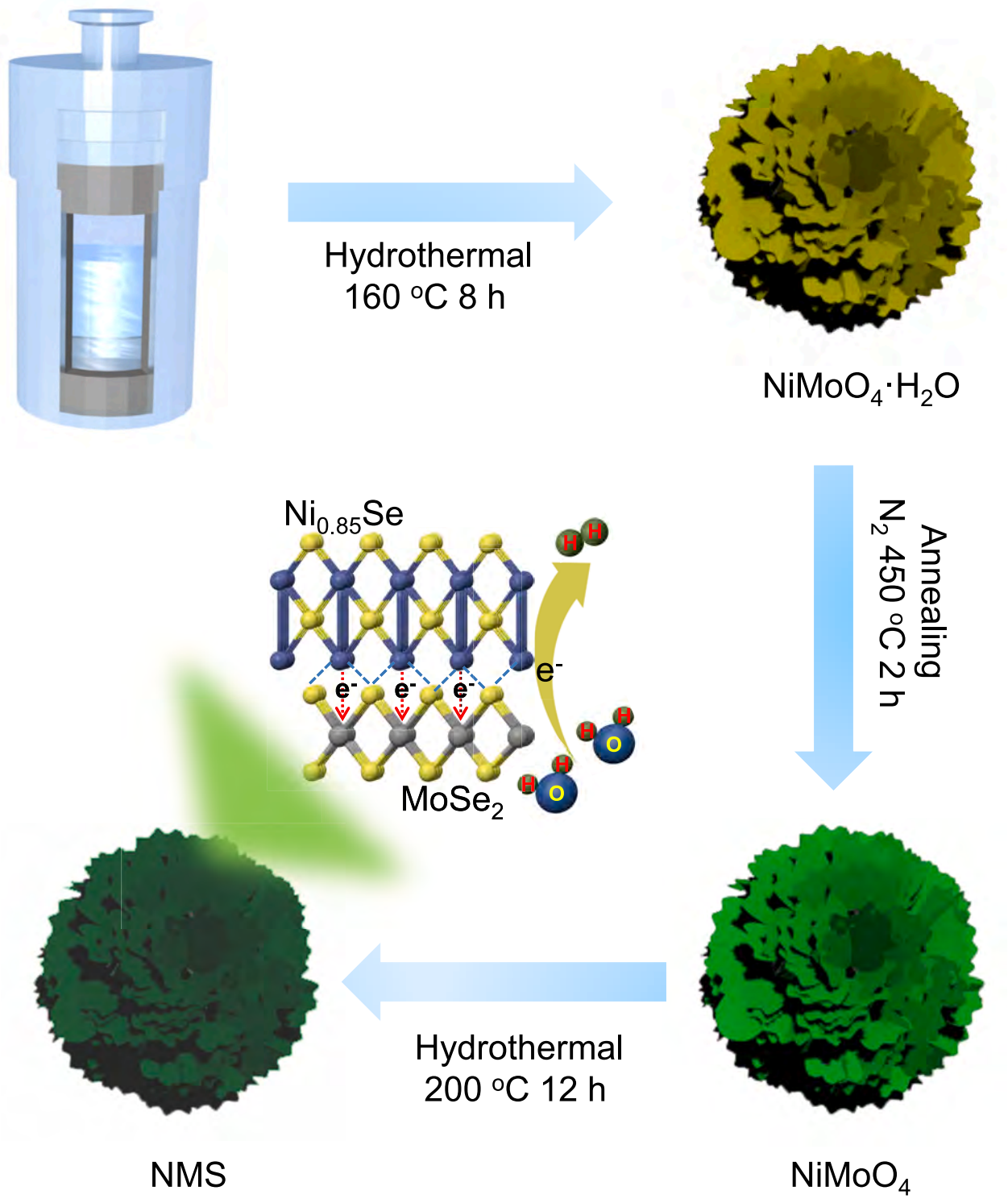

Scheme 1. Schematic illustration of the preparation of NiMo selenides (NMS) composite and the application for HER.

significant role in HER. For example, Ni^{2+} has been identified to be a suitable candidate for high-performance HER [25]. Zhan et al. [26] have manipulated the phase composition and charge state of the Ni species and found that a lower Ni charge state improves the HER activity. However, how to synergistically integrate the effects of the electronic interactions between Ni and Mo and tuning of the oxidation states has not been extensively studied because the task is quite challenging.

Herein, a hydrothermal selenation technique is designed to regulate the electronic structure of NiMo selenides composite nanosheets and simultaneously modulate the oxidation states by programmed reduction, as illustrated in Scheme 1. The electronic interactions between Ni and Mo produced by *in situ* phase separation and pertaining mechanism are investigated. The NiMo selenides composite electrocatalyst requires a mere overpotential of 124 mV to achieve a current density of 10 mA cm^{-2}. The Tafel slope and Faradaic efficiency for hydrogen production are 63 mV dec^{-1} and 98.9 %, respectively. The materials also have robust stability that is corroborated by continuous operation for 170 h. Our results reveal a valuable strategy to design and fabricate non-

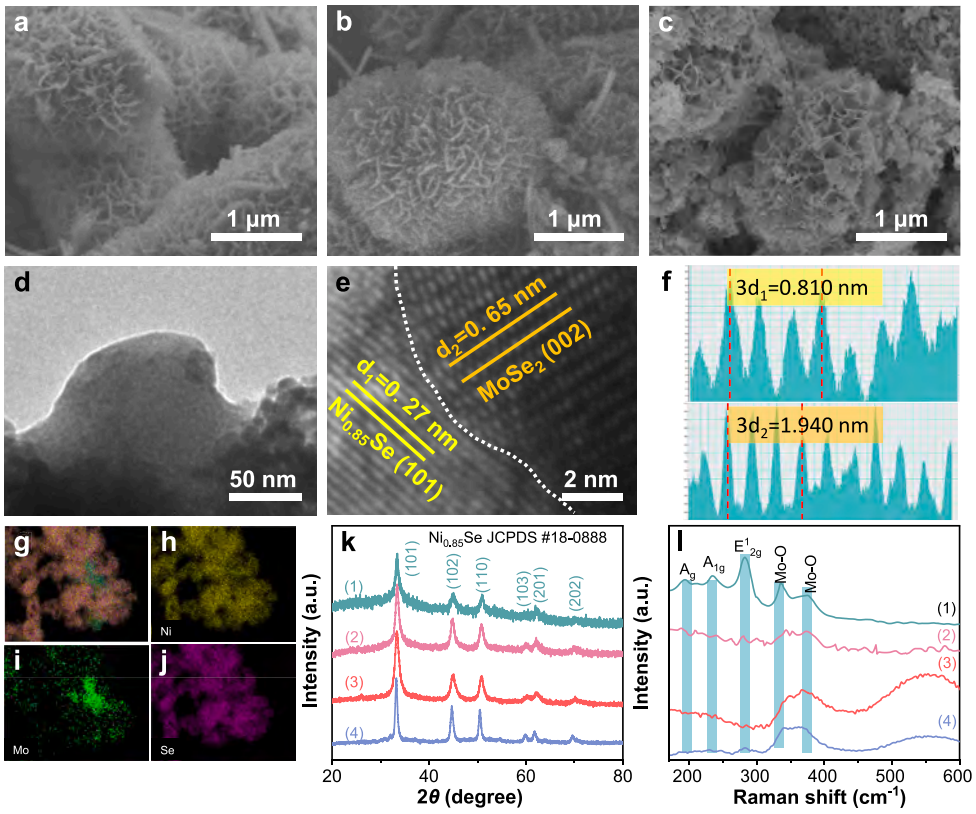

Fig. 1. SEM images of (a) $NiMoO_4{\cdot}xH_2O$, (b) $NiMoO_4$, and (c) NMS-3; (d) TEM image, (e) HR-TEM image, and (f) Lattice image of NMS-3; (g-j) Elemental maps of NMS-3; (k) XRD patterns and (l) Raman scattering spectra of (1) NMS-1, (2) NMS-2, (3) NMS-3, and (4) NMS-4.

precious transition metal-based electrocatalysts for efficient alkaline HER.

2. Experiment details

2.1. Materials preparation

9 mmol nickel chloride ($NiCl_2{\cdot}6H_2O$), 9 mmol sodium molybdate ($Na_2MoO_4{\cdot}2H_2O$), and 30 mmol NH_4F were dissolved in 150 mL of deionized water (DW) and 150 mL ethanol under stirring. It was transferred to a 500 mL autoclave and heated to 160 °C for 4 h, followed by washing with DW three times and freeze-drying for more than 48 h. The $NiMoO_4$ nanosheets were obtained by calcining the sample at 450 °C for 1 h at a ramping rate of 2 °C min^{-1} in a nitrogen atmosphere.

NMS composite was synthesized by a hydrothermal reaction with Se powder as the precursor. The 0.500 mmol Se powder was dissolved in 1 mL of $N_2H_4{\cdot}H_2O$, stirred for 30 min, and aged for 24 h. The Se-$N_2H_4{\cdot}H_2O$ solution, 0.125–0.500 mmol $NiMoO_4$, and 20 mmol NH_4F were added to 30 mL of DW and stirred for another 30 min. The mixture was then transferred to a 50 mL Teflon-lined stainless-steel autoclave and kept at 180 °C for 12 h. The product was collected, washed with DW several times, and freeze-dried. The samples prepared with 0.125, 0.250, 0.375, and 0.500 mmol $NiMoO_4$ were designated as NMS-1, NMS-2, NMS-3, and NMS-4, respectively. To synthesize the pure $MoSe_2$ (MS) and $Ni_{0.85}Se$ (NS), the same protocols used for NMS-3 were adopted but without the nickel or molybdenum source in the initial hydrothermal reaction.

2.2. Materials characterization

The morphology of the samples was examined by scanning electron microscopy (SEM, Hitachi SU 3500) and transmission electron microscopy (TEM, Titan G260-300) equipped with energy-dispersive X-ray spectrometry (EDS). The crystal structure and composition were characterized by X-ray diffraction (XRD, LabX XRD-6100, Shimadzu), high-resolution TEM (HR-TEM), Raman scattering (HR RamLab), and X-ray photoelectron spectroscopy (XPS, Thermo Scientific K-Alpha, Thermo Fisher) using a monochromatic Al Kα X-ray source.

2.3. Electrochemical measurements

The working electrode was a modified glassy carbon electrode (GCE, 3 mm in diameter) loaded with the as-prepared samples. 20 mg of the electrocatalyst was dispersed in 5 mL DW ultrasonically to form the ink and 2 μL of the ink was drop-casted on a clean GCE and dried. The Nafion solution (5 wt%, 5 μL) was used to cover the GCE. The electrochemical measurements were performed on a CHI 660E electrochemical workstation using a standard three-electrode system in a 1.0 M KOH aqueous solution. The Hg/HgO electrode was the reference electrode and the graphite rod served as the counter electrode. All the potentials were *iR* corrected and calibrated to the reversible hydrogen electrode (RHE) according to the Nernst equation: $E_{RHE} = E_{Hg/HgO} + 0.098 + 0.059 \times pH$, where the pH of the 1.0 M KOH aqueous solution was measured to be 13.63 by a pH meter (FE28, Mettler Toledo). Linear sweep voltammetry (LSV) was conducted at a scanning rate of 5 mV s^{-1}. The Tafel slopes were obtained by plotting the overpotentials (η) *vs.* log currents (log $|j|$) derived from the polarization curves. The electrochemically active surface areas (ECSA) were determined by measuring the electrochemical double-layer capacitance (C_{dl}) of the electrocatalysts based on the cyclic voltammetry (CV) curves in the potential range from −0.4 to −0.5 V *vs.* Hg/HgO electrode at different scanning rates of 10–100 mV s^{-1}. Electrochemical impedance spectroscopy (EIS) was carried out at an initial potential of −0.22 V *vs.* RHE and the stability was assessed by the chronoamperometric method at a constant potential.

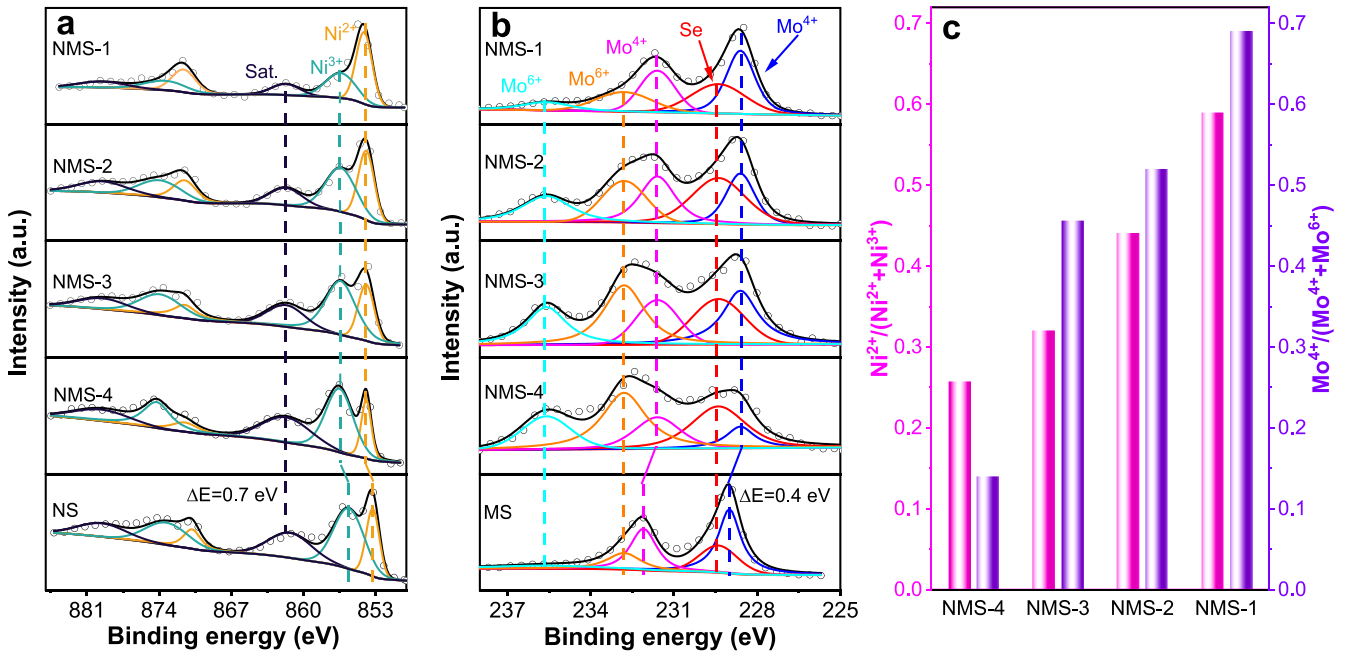

Fig. 2. High-resolution XPS spectra of (a) Ni-2*p* and (b) Mo-3*d*; (c) Calculated ratios of Ni^{2+} / (Ni^{2+} + Ni^{3+}) and Mo^{4+} / (Mo^{4+} + Mo^{6+}) of the NMS composites.

3. Results and discussion

3.1. Structure of the electrocatalysts

Scheme 1 illustrates the preparation of NMS composite nanosheets by a two-step hydrothermal process and HER application. After preparing the $NiMoO_4{\cdot}xH_2O$ precursor by the first hydrothermal reaction, the sample is annealed to remove water and stabilize the structure to produce $NiMoO_4$. Afterwards, a second hydrothermal process using Se powders as a source is performed to convert $NiMoO_4$ into selenide, during which phase separation occurs to produce the NMS composite. As a result of the interactions between the phases and the electron transfer effect of Ni and Mo atoms, the electronic configuration of the surface sites is modulated and at the same time, the hydrogen adsorption behavior which impacts the HER activity is altered.

The SEM image in Fig. 1**a** shows the hierarchical $NiMoO_4{\cdot}xH_2O$ precursor consisting of uniform nanosheets. After annealing at 450 °C to remove water, the nanosheet structure is retained for the $NiMoO_4$, as indicated by the SEM image in Fig. 1**b.** Because of the unstable structure of the $NiMoO_4{\cdot}xH_2O$ precursor in alkaline media, it is necessary to anneal the $NiMoO_4{\cdot}xH_2O$ to enhance its structure stability before further hydrothermal for selenation [27,28]. After the ensuing hydrothermal reaction at 180 °C for 12 h, the hierarchical sphere assembled of nanosheet structure is preserved as shown in Fig. 1**c**. The morphology of the samples with different (NiMo)/Se ratios used in hydrothermal selenation is shown in **Figure S1**. The surface of NMS-1 and NMS-2 was covered by particles, which may be the excess Se since the ratio of $NiMoO_4$:Se precursors is small in these samples. The open structure between the nanosheets in the sphere provides a large surface area for exposure to the active site and also allows electrolytes to enter the interior [29–32].

The TEM image in Fig. 1**d** confirms the nanosheet structure. The HR-TEM image in Fig. 1**e-f** discloses interplanar distances of 0.27 and 0.65 nm ascribed to the (1 0 1) planes of $Ni_{0.85}Se$ and (0 0 2) planes of $MoSe_2$, respectively. Atomic distortion is observed from the interface of the $Ni_{0.85}Se$ and $MoSe_2$ phases as indicated by the dotted line, possibly resulting in the electronic structure modulation [33,34]. The elemental maps in Fig. 1**g-j** reveal uniform distributions of the Mo, Se, and Ni.

The crystal structure and phase composition of the samples are examined by XRD and Raman scattering. The XRD pattern of the initial hydrothermal product in **Figure S2** matches that of $NiMoO_4{\cdot}xH_2O$ (JCPDS card No. 13-0128) consistent with a previous report [35]. After annealing at 450 °C, the $NiMoO_4{\cdot}xH_2O$ precursor is converted into $NiMoO_4$ (JCPDS card No. 45-0142) that the peaks at 23.3°, 26.5°, 28.4°, 27.1°, 46.6°, and 43.7° are associated with the (0 2 1), (2 2 0), (3 1 1), (1 1 2), (4 2 2), and (2 4 1) planes of monoclinic $NiMoO_4$ (**Figure S3**). After the second hydrothermal selenation reaction (Fig. 1**k**), the diffraction peaks observed from the NMS samples at 33.1°, 44.9°, 50.4°, 60.2°, 61.7°, and 69.6° arise from the (1 0 1), (1 0 2), (1 1 0), (1 0 3), (2 0 1), and (2 0 2) planes of $Ni_{0.85}Se$ (JCPDS card No. 18-0888). The XRD patterns of the pure-phase samples in **Figure S4** suggest the presence of pure $Ni_{0.85}Se$ (JCPDS card No. 18-0888) and $MoSe_2$ (JCPDS card No. 29-0914), respectively.

The Raman scattering spectrum of $NiMoO_4$ in **Figure S5** exhibits peaks at 952, 905, 819, 704, and 384 cm^{-1} corresponding to vibrations of $NiMoO_4$ [36]. After hydrothermal selenation, distinct Raman peaks emerge at ~235 and ~282 cm^{-1} attributable to the A_{1g} and E^1_{2g} vibration modes of $MoSe_2$ (Fig. 1**l and S6**), thus corroborating the formation of $MoSe_2$ in the products [37]. The peak at around 200 cm^{-1} is assigned to Ni-Se vibration (Fig. 1**l**) [38,39] and the two peaks in **Figures S6 and 1l** at 336 and 379 cm^{-1} stem from Mo—O and Mo═O bending [40]. The Raman scattering spectrum of the pure phase of $Ni_{0.85}Se$ in **Figure S7** shows two weak and broad peaks at 192 cm^{-1} and 521 cm^{-1}, corresponding to Ni-Se stretching [38,39]. Raman scattering confirms the presence of $MoSe_2$ and $Ni_{0.85}Se$ in the NMS composite.

Figure S8a presents the XPS survey spectrum of $NiMoO_4$ showing the existence of Ni, O, and Mo. The Ni-2*p* spectrum can be divided into four peaks (**Figure S8b**) with the peaks at 856.3 and 874.0 eV corresponding to Ni-$2p_{3/2}$ and Ni-$2p_{1/2}$ of Ni^{2+} and those at 862.0 and 879.7 eV being the satellite signals. The Mo-3*d* spectrum shows peaks at 232.1 and 235.2 eV for Mo-$3d_{5/2}$ and Mo-$3d_{3/2}$ of Mo^{6+} (**Figure S8c**) [41].

The survey spectra of all the NMS composites in **Figure S9** show the Ni-2*p*, Mo-3*d*, Se-3*d*, and O-1*s* peaks. The O-1*s* signal may result from slight surface oxidation which has been observed independently [42,43]. The chemical states of Ni and Mo in the NMS composites are shown in Fig. 2**a-b**. The Ni-2*p* spectra can be deconvoluted into two doublets ($2p_{3/2}$ and $2p_{1/2}$) together with two shake-up satellite peaks due to the spin–orbit coupling effect [44]. Specifically, the $2p_{3/2}$ peak

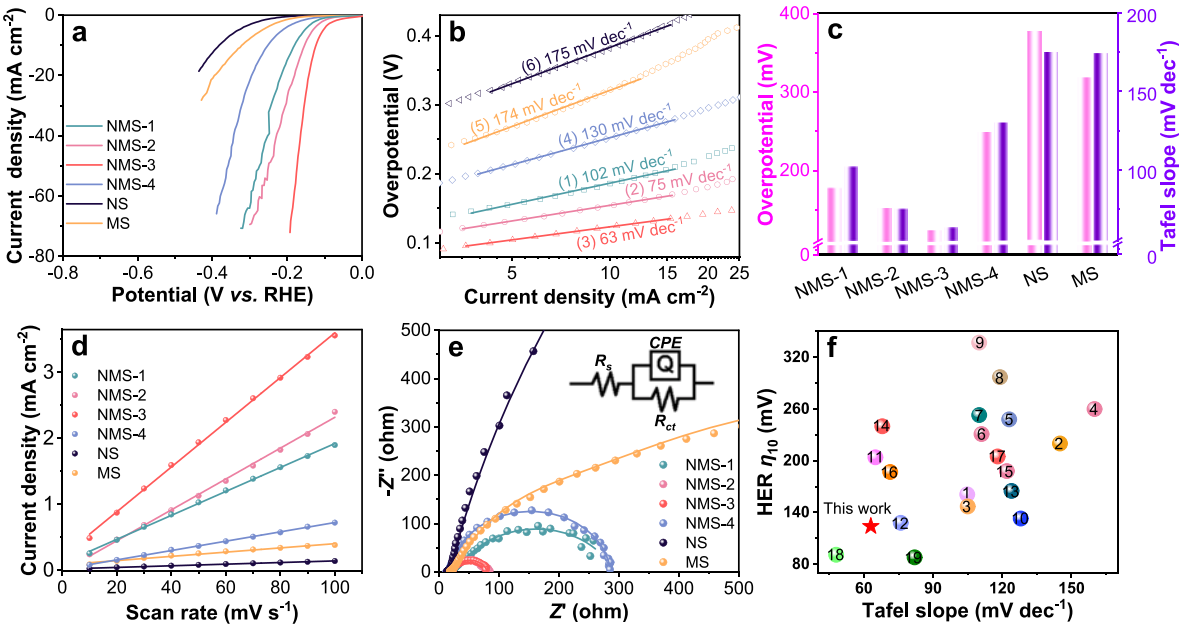

Fig. 3. HER properties of (1) NMS-1, (2) NMS-2, (3) NMS-3, (4) NMS-4, (5) MS, and (6) NS modified GCE in 1.0 M KOH: (a) Polarization curves; (b) Tafel plots; (c) Summary of the overpotentials at 10 mA cm^{-2} (pink) and Tafel slopes (purple); (d) Double-layer capacitance (C_{dl}) plots; (e) Nyquist plots; (f) Comparison of the HER characteristics with those of recently reported electrocatalysts including (1) Ni/Mo_xC [54], (2–3) NiS and NiS_2 [45], (4) EG/$Co_{0.85}Se$/NiFe-LDH [55], (5) $MoSeS_2$-x [56], (6–9) $Ni_{0.9}Fe_{0.1}$/NC, $Ni_{0.8}Fe_{0.2}$/NC, $Ni_{0.7}Fe_{0.3}$/NC, and $Ni_{0.6}Fe_{0.4}$/NC [57], (10) $NiSe_2$/CC-180 [46], (11) NiS_2/MoS_2 HNW [58], (12) 2D-MoS_2/$Co(OH)_2$ [59], (13) Co/M−MoS_2 [60], (14) Co-1T-MoS_2 [61], (15) Ni-Mo co-doped WSe_2 [62], (16) NiMOF-derived $MoSe_2$@$NiSe_2$ [63], (17) NiCo-WSe_2 [64], (18) NiMoSe/NF-1 [65], and (19) Mo,S-co-doped NiSe/NF [66].

can be further divided into two subpeaks at 853.9 and 856.3 eV for Ni^{2+} and Ni^{3+} [45,46]. Similarly, the $2p_{1/2}$ peak can be resolved into two peaks of 871.5 and 873.9 eV for Ni^{2+} and Ni^{3+}, respectively [45,46]. As shown in Fig. 2**b**, the Mo-3*d* spectrum shows five peaks, among which those at 232.8 and 235.6 eV belong to Mo-$3d_{5/2}$ and Mo-$3d_{3/2}$ of Mo^{6+}, those at 228.6 and 231.6 eV belong to Mo-$3d_{5/2}$ and Mo-$3d_{3/2}$ of Mo^{4+} [37,47], and that at 229.4 eV is Se-3*s*, consistent with the literature [48]. In addition, the high-resolution XPS Se-3*d* spectra of composites are shown in **Figure S10**. The peaks at 54.7 and 55.7 eV corresponded to Se-$3d_{5/2}$ and Se-$3d_{3/2}$, respectively, confirming the presence of Se^{2-} [49]. As is shown in **Figure S11**, the high-resolution XPS O-1*s* spectra of NMS-x showed two distinct peaks located at 531.4 and 532.8 eV, corresponding to the oxygen in metal oxide species (M−O) and surface-adsorbed O species (O_{ad}), respectively [50,51].

Compared to the Ni-2*p* and Mo-3*d* spectra of pure $Ni_{0.85}Se$ and $MoSe_2$ in Fig. 2**a-b**, the binding energies of both Ni^{2+} and Ni^{3+} in the NMS composites shift to higher binding energies by 0.7 eV, whereas the peaks of Mo-3*d* of Mo^{4+} in the NMS composites shift to lower binding energies by 0.4 eV, implying electron transfer from Ni to Mo in the composite phases [42,52,53]. The electronic interaction between the Ni and Mo atoms modulates the hydrogen adsorption behavior of the active sites. Especially, the Mo sites with rich electrons have superior reduction properties. Furthermore, as the (NiMo)/Se ratio of the NMS composites decreases, the $Ni^{2+}/(Ni^{2+} + Ni^{3+})$ and $Mo^{4+}/(Mo^{4+} + Mo^{6+})$ ratios increase as indicated in Fig. 2**c**. Generally, the ionic Ni and Mo are reduced by the Se-N_2H_4 reducing agent. The smaller the (NiMo)/Se ratio, the larger the Se-N_2H_4 precursor content. Therefore, more Se-N_2H_4 in the precursor reduces Ni and Mo to lower valences, indicating the selective reduction of the NiMo species. The results suggest that the chemical states of Ni and Mo can be regulated by adjusting the (NiMo)/Se ratio of the precursor. Normally, the Ni-based electrocatalyst with a lower Ni oxidation state facilitates HER [25,26] and hence, this dual regulation strategy encompassing the electronic structure interaction between Ni and Mo atoms at the interface and selective reduction of the NiMo species to alter the oxidation states optimizes the electronic configuration of the active sites to foster the HER activity.

3.2. HER performance

The NMS composite-modified GCE is used as the working electrode to evaluate the HER performance in the 1.0 M KOH aqueous solution. Fig. 3**a** shows the polarization curves and enhanced HER activity of the NMS composites compared to the pure $MoSe_2$ and $Ni_{0.85}Se$. For example, NMS-3 requires an overpotential of 124 mV to achieve a current density of 10 mA cm^{-2}, which is smaller than those of NMS-1 (178 mV), NMS-2 (152 mV), NMS-4 (249 mV), NS (377 mV), and MS (318 mV). Fig. 3**b** shows that the Tafel slope of NMS-3 (63 mV dec^{-1}) is smaller than those of NMS-2 (75 mV dec^{-1}), NMS-1 (102 mV dec^{-1}), NMS-4 (130 mV dec^{-1}), MS (174 mV dec^{-1}), and NS (175 mV dec^{-1}), suggesting faster kinetics for NMS-3. Fig. 3**c** illustrates the overpotentials to produce a current density of 10 mA cm^{-2} and Tafel slopes confirming the superiority of NMS-3 as a HER electrocatalyst. The high HER activity of NMS-3 results from the optimized electronic structure and balanced hydrogen adsorption capability at the active sites, which are achieved by oxidation states tuning and exploiting the electronic interaction between Ni and Mo at the NiMo selenides composite interface [26].

The HER activity depends on the ECSA, which is reflected by the C_{dl} derived from the cyclic voltammetry curves in the non-Faraday region, as shown in **Figure S12**. Fig. 3**d** shows that the C_{dl} of NMS-3 is 33 mF cm^{-2}, which is 1.4 times, 1.8 times, 4.7 times, 11 times, and 33 times larger than those of NMS-2 (23 mF cm^{-2}), NMS-1 (18 mF cm^{-2}), NMS-4 (7 mF cm^{-2}), MS (3 mF cm^{-2}), and NS (1 mF cm^{-2}), respectively. The largest ECSA of NMS-3 should result from the optimal balance of surface morphology with large abundant active site exposure and highly intrinsic catalytic activity of the active Ni^{2+} and Mo^{4+} sites compared to the others. Generally, a larger C_{dl} implies more electrochemically active site exposure. The electronic interactions between Ni and Mo atoms tune the electronic configuration of the active sites, and Ni^{2+} has been reported to enhance HER activity [26]. Therefore, the larger ECSA of NMS-3 stems from the synergistic dual-regulation effects of electronic interactions and oxidation states of Ni and Mo, leading to the activation of more surface sites. The turnover frequency (TOF) is studied to evaluate the intrinsic electrocatalytic capability of the NMS composites

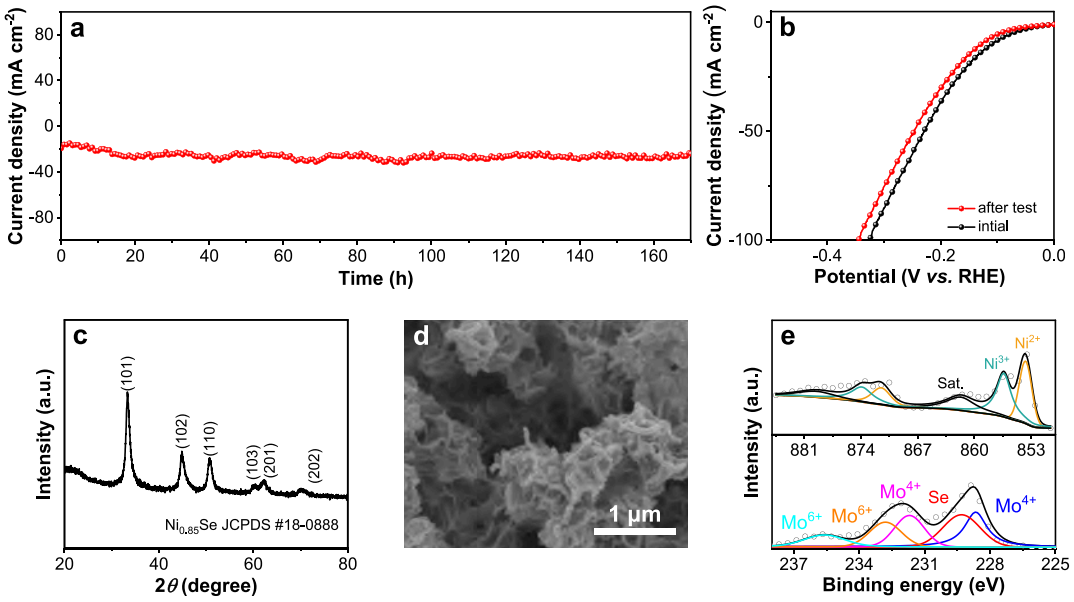

Fig. 4. (a) Stability test; (b) Polarization curves of NMS-3 before and after the long-term test; (c) XRD, (d) SEM image, and (e) High-resolution XPS Ni-2*p* and Mo-3*d* spectra of NMS-3 after the long-term test.

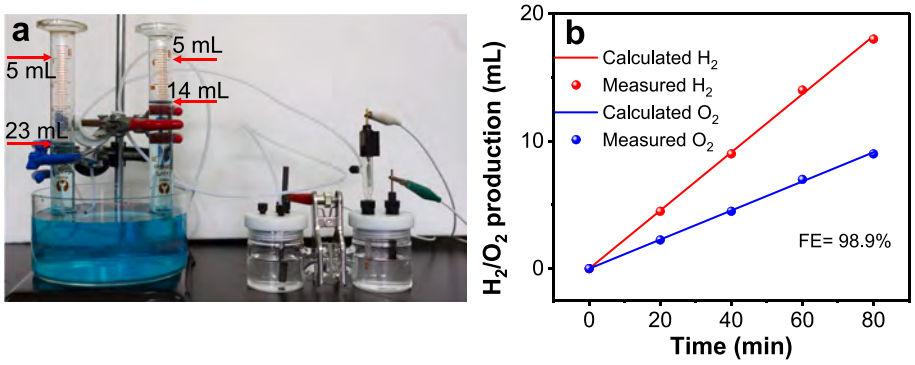

Fig. 5. (a) Photograph of the collection and volume determination apparatus for H_2 and O_2 by the water displacement method; (b) Experimental and theoretical amounts of H_2 and O_2 produced by NMS-3 at a current of 30 mA in 1.0 M KOH.

(**Supporting note I**). The NMS-3 shows a TOF of 1.0 s^{-1} at an overpotential of 137 mV, which is larger than that of the other electrocatalysts, confirming the excellent intrinsic electrocatalytic activity (**Figure S13**).

The charge transfer resistance (R_{ct}) of the electrocatalysts in HER is determined by EIS, as shown in Fig. 3**e**. NMS-3 has a smaller R_{ct} than NMS-1, NMS-2, and NMS-4, reflecting faster HER kinetics. The comparison of the hydrogen evolution characteristics of the NMS composite electrocatalyst in this work and other non-precious transition metal-based electrocatalysts at 10 mA cm^{-2} is shown in Fig. 3**f** and listed in **Table S1**, suggesting that the NMS/CC is superior to those of the typical transition metal-based sulfides and selenides.

Stability is an important parameter in commercial applications. The durability of NMS-3 is evaluated by chronoamperometry at a potential of −0.15 V *vs.* RHE, as shown in Fig. 4**a**. Negligible changes are observed from the current densities after continuous operation for 170 h. Additionally, only a 14 mV shift in the potential is observed from the LSV curve at a current density of 10 mA cm^{-2} after the long-term test in comparison with the initial LSV curve (Fig. 4**b**), indicating that NMS-3 is extremely stable in alkaline HER. The composition and morphology of NMS-3 after the long-term test are investigated. Fig. 4**c** reveals diffraction peaks from $Ni_{0.85}Se$ (JCPDS card No. 18–0888) matching the pristine sample. The hierarchical structure composed of nanosheets is also preserved as shown by Fig. 4**d**. The XPS survey in **Figure S14** discloses the presence of Ni and Mo. High-resolution XPS Ni-2*p* and Mo-3*d* spectra in Fig. 4**e** show similar peaks as the original sample. The ratios of Ni^{2+} / (Ni^{2+} + Ni^{3+}) and Mo^{4+} / (Mo^{4+} + Mo^{6+}) are calculated to be 0.31 and 0.47, respectively, which are very close to those of the fresh sample of 0.32 and 0.46. In addition, there are no differences in the binding energy of both Ni and Mo elements before and after the long-term test. The results provide strong evidence of the excellent durability of NMS-3 in alkaline HER.

The Faradaic efficiency of NMS-3 in HER is determined by the water displacement method illustrated in Fig. 5**a** by collecting H_2 from the working electrode and O_2 from the counter electrode using cylinders in a three-electrode system with a graphite rod as counter electrode, NMS-3 as working electrode, and Hg/HgO as reference electrode. Fig. 5**b** shows that 18 mL of H_2 and 9 mL of O_2 are generated in 80 min at a current of 30 mA. The Faradaic efficiency is calculated to be 98.9 % which is close to the limit of 100 %.

4. Conclusions

NiMo selenides composite heterostructure composites are synthesized by a dual-regulation strategy. The electronic structure of Ni and Mo on the surface is modulated by the electronic interactions between

Ni and Mo, where electrons are transferred from Ni to Mo at the heterointerface due to the *in-situ* phase separation of $Ni_{0.85}Se$ and $MoSe_2$. Furthermore, the oxidation states of Ni and Mo are altered by selective reduction using a programmed hydrothermal selenation process, which optimizes the amount of highly active Ni^{2+} species in the electrocatalyst. The dual-regulation strategy produces outstanding HER properties such as an overpotential of 124 mV for a current density of 10 mA cm^{-2}, a small Tafel slope of 63 mV dec^{-1}, robust stability for 170 h, and high Faradaic efficiency of 98.9 % in hydrogen production. This dual-regulation technique can be extended to the design and fabrication of other types of low-cost transition metal-based heterostructured electrocatalysts for various applications.

CRediT authorship contribution statement

Rong Li: Methodology, Formal analysis, Investigation, Visualization, Roles/Writing - original draft. **Song Xie:** Methodology, Formal analysis, Investigation, Visualization, Roles/Writing – original draft. **Yujie Zeng:** Investigation, Visualization, Data curation, Formal analysis. **Qiangqiang Zhao:** Methodology, Investigation, Visualization. **Yaping Miao:** Data curation, Investigation, Visualization. **Zhitian Liu:** Writing – review & editing, Supervision, Visualization. **Paul K. Chu:** Funding acquisition, Writing – review & editing, Visualization. **Xiang Peng:** Conceptualization, Funding acquisition, Supervision, Writing – review & editing, Visualization, Project administration.

Declaration of Competing Interest

The authors declare that they have no known competing financial interests or personal relationships that could have appeared to influence the work reported in this paper.

Data availability

Data will be made available on request.

Acknowledgements

This work was financially supported by the National Natural Science Foundation of China (52002294), Key Research and Development Program of Hubei Province (2021BAA208), Knowledge Innovation Program of Wuhan-Shuguang Project (2022010801020364), the Graduate Innovative Fund of Wuhan Institute of Technology (CX2022226), City University of Hong Kong Donation Research Grants (DON-RMG 9229021 and 9220061), as well as City University of Hong Kong Strategic Research Grant (SRG) (7005505).

Appendix A. Supplementary material

Supplementary data to this article can be found online at https://doi.org/10.1016/j.fuel.2023.130203.

References

[1] Chu S, Cui Y, Liu N. The path towards sustainable energy. Nat Mater 2017;16(1):16–22. https://doi.org/10.1038/nmat4834.
[2] Yuan Y, Lei AW. Electrochemical Oxidative Cross-Coupling with Hydrogen Evolution Reactions. Acc Chem Res 2019;52:3309–24. https://doi.org/10.1021/acs.accounts.9b00512.
[3] Wu T, Sun MZ, Huang BL. Non-noble metal-based bifunctional electrocatalysts for hydrogen production. Rare Metals 2022;41:2169–83. https://doi.org/10.1007/s12598-021-01914-x.
[4] Chen HX, Xu H, Song ZR, Liu Y, Cui H, Gao JK. Pressure-induced bimetallic carbon nanotubes from metal–organic frameworks as optimized bifunctional electrocatalysts for water splitting. Rare Metals 2023;42:155–64. https://doi.org/10.1007/s12598-022-02121-y.
[5] Shi YM, Zhang B. Recent advances in transition metal phosphide nanomaterials: synthesis and applications in hydrogen evolution reaction. Chem Soc Rev 2016;45:1529–41. https://doi.org/10.1039/C5CS00434A.
[6] Peng X, Jin X, Gao B, Liu ZT, Chu PK. Strategies to improve cobalt-based electrocatalysts for electrochemical water splitting. J Catal 2021;398:54–66. https://doi.org/10.1016/j.jcat.2021.04.003.
[7] Hao R, Feng Q-L, Wang X-J, Zhang Y-C, Li K-S. Morphology-controlled growth of large-area $PtSe_2$ films for enhanced hydrogen evolution reaction. Rare Metals 2022;41:1314–22. https://doi.org/10.1007/s12598-021-01877-z.
[8] Zhang RB, Tu ZA, Meng S, Feng G, Lu ZH, Yu YZ, et al. Engineering morphologies of yttrium oxide supported nickel catalysts for hydrogen production. Rare Metals 2023;42:176-188. https://doi.org/10.1007/s12598-022-02136-5.
[9] Huang JZ, Han JC, Wu T, Feng K, Yao T, Wang XJ, et al. Boosting Hydrogen Transfer during Volmer Reaction at Oxides/Metal Nanocomposites for Efficient Alkaline Hydrogen Evolution. ACS Energy Lett 2019;4:3002–10. https://doi.org/10.1021/acsenergylett.9b02359.
[10] Han QL, Luo YH, Liu GH, Wang YJ, Li JD, Chen ZW. Comparative study on the distinct activity for NiFe-based phosphide and sulfide pre-electrocatalysts towards hydrogen evolution reaction. J Catal 2022;413:425–33. https://doi.org/10.1016/j.jcat.2022.06.039.
[11] Lee Y-H, Zhang X-Q, Zhang WJ, Chang M-T, Lin C-T, Chang K-D, et al. Synthesis of Large-Area MoS_2 Atomic Layers with Chemical Vapor Deposition. Adv Mater 2012;24:2320–5. https://doi.org/10.1002/adma.201104798.
[12] Li JD, Li K, Tang QL, Liang JX, Bao CY, Shi F, et al. Structure phase engineering strategy through acetic acid coupling to boost hydrogen evolution reaction performance of 2H phase MoS_2 at wide pH range. Fuel 2023;347:128428. https://doi.org/10.1016/j.fuel.2023.128428.
[13] Jun YJ, Kim J, Kim SY, Ahn SH. Low-crystalline NiCuP with elemental synergy for hydrogen evolution reaction in proton exchange membrane water electrolyzer. Fuel 2023;350:128737. https://doi.org/10.1016/j.fuel.2023.128737.
[14] Niu SY, Yang ZW, Qi FG, Han Y, Shi ZZ, Qiu QW, et al. Electrical Discharge Induced Bulk-to-Nanoparticle Transformation: Nano High-Entropy Carbide as Catalysts for Hydrogen Evolution Reaction. Adv Funct Mater 2022;32:2203787. https://doi.org/10.1002/adfm.202203787.
[15] Fang XJ, Ren LP, Li F, Jiang ZX, Wang ZG. Modulating electronic structure of $CoSe_2$ by Ni doping for efficient electrocatalyst for hydrogen evolution reaction. Rare Metals 2022;41:901–10. https://doi.org/10.1007/s12598-021-01819-9.
[16] Peng X, Pi CR, Zhang XM, Li S, Huo KF, Chu PK. Recent progress of transition metal nitrides for efficient electrocatalytic water splitting. Sustain Energ Fuels 2019;3:366. https://doi.org/10.1039/c8se00525g.
[17] Luo ZY, Li JJ, Li YL, Wu DJ, Zhang L, Ren XZ, et al. Band Engineering Induced Conducting 2H-Phase MoS_2 by Pd-S-Re Sites Modification for Hydrogen Evolution Reaction. Adv Energy Mater 2022;12:2103823. https://doi.org/10.1002/aenm.202103823.
[18] Peng X, Yan YJ, Jin X, Huang C, Jin WH, Gao B, et al. Recent advance and prospectives of electrocatalysts based on transition metal selenides for efficient water splitting. Nano Energy 2020;78:105234. https://doi.org/10.1016/j.nanoen.2020.105234.
[19] Mao S, Wen Z, Ci S, Guo X, Ostrikov K, Chen J. Perpendicularly oriented $MoSe_2$/graphene nanosheets as advanced electrocatalysts for hydrogen evolution. Small 2015;11:414–9. https://doi.org/10.1002/smll.201401598.
[20] Zheng HY, Li YJ, Liu HB, Yin XD, Li YL. Construction of heterostructure materials toward functionality. Chem Soc Rev 2011;40:4506–24. https://doi.org/10.1039/c0cs00222d.
[21] Xiong LW, Qiu YF, Peng X, Liu ZT, Chu PK. Electronic structural engineering of transition metal-based electrocatalysts for the hydrogen evolution reaction. Nano Energy 2022;104:107882. https://doi.org/10.1016/j.nanoen.2022.107882.
[22] Tian YL, Zhang X, Dou SL, Zhang LP, Zhang H, Lv HM, et al. A comprehensive study of electrochromic device with variable infrared emissivity based on polyaniline conducting polymer. Sol Energy Mater Sol Cells 2017;170:120–6. https://doi.org/10.1016/j.solmat.2017.05.053.
[23] Zhang X, Zhang Y-Y, Zhang Y, Jiang W-J, Zhang Q-H, Yang Y-G, et al. Phase-Controlled Synthesis of 1T-$MoSe_2$/NiSe Heterostructure Nanowire Arrays via Electronic Injection for Synergistically Enhanced Hydrogen Evolution. Small Methods 2019;3:1800317. https://doi.org/10.1002/smtd.201800317.
[24] Ren ZF, Zhou H, Yu F, Huang Y, Sun J, Zhu Z, et al. Efficient hydrogen evolution by ternary molybdenum sulfoselenide particles on self-standing porous nickel diselenide foam. Nat Commun 2016;7:12765. https://doi.org/10.1038/ncomms12765.
[25] Moroto K, Miyake K, Shu Y, Toyama Y, Ma JJ, Tanaka S, et al. Fabrication of NiS_x/C with a tuned S/Ni molar ratio using Ni^{2+} ions and Amberlyst for hydrogen evolution reaction (HER). Int J Hydrogen Energ 2020;45:24567–72. https://doi.org/10.1016/j.ijhydene.2020.06.043.
[26] Zhan TR, Tan L, Yu JT, Wang HY, Gao HT, Liu X, et al. Controllable synthesis and phase-dependent catalytic performance of dual-phase nickel selenides on Ni foam for overall water splitting. Appl Catal B-Environ 2022;303:120915. https://doi.org/10.1016/j.apcatb.2021.120915.
[27] Zhu JY, Liu C, Cui SW, Lu ZR, Ye YJ, Wen JY, et al. Multistep Dissolution of Lamellar Crystals Generates Superthin Amorphous $Ni(OH)_2$ Catalyst for UOR. Adv Mater 2023;35:2301549. https://doi.org/10.1002/adma.202301549.
[28] Liu X, Meng JS, Ni K, Guo RT, Xia FJ, Xie JJ, et al. Complete Reconstruction of Hydrate Pre-Catalysts for Ultrastable Water Electrolysis in Industrial-Concentration Alkali Media. Cell Rep Phys Sci 2020;1:100241. https://doi.org/10.1016/j.xcrp.2020.100241.
[29] Qing C, Liu YN, Sun XP, OuYang XX, Wang H, Sun D, et al. Controlled growth of $NiMoO_4{\cdot}H_2O$ nanoflake and nanowire arrays on Ni foam for superior performance of asymmetric supercapacitors. RSC Adv 2016;6:67785–93. https://doi.org/10.1039/c6ra13483a.

[30] Wei FX, Li YX, Wang H, Shu T, Yuan JZ, Lu GG, et al. Comparative research of hierarchical CoS_2@C and Co_3S_4@C nanosheet as advanced supercapacitor electrodes. J Energy Storage 2023;60:106551. https://doi.org/10.1016/j.est.2022.106551.
[31] Yang LM, Yang T, Wang EH, Yu XT, Wang K, Du ZT, et al. Bifunctional hierarchical NiCoP@FeNi LDH nanosheet array electrocatalyst for industrial-scale high-current-density water splitting. J Mater Sci Technol 2023;159:33–40. https://doi.org/10.1016/j.jmst.2023.02.050.
[32] Guan C, Liu JP, Cheng CW, Li HX, Li XL, Zhou WW, et al. Hybrid structure of cobalt monoxide nanowire@nickel hydroxidenitrate nanoflake aligned on nickel foam for high-rate supercapacitor. Energy Environ Sci 2011;4:4496–9. https://doi.org/10.1039/C1EE01685G.
[33] Zheng XR, Han XP, Cao YH, Zhang Y, Nordlund D, Wang JH, et al. Identifying Dense $NiSe_2$/$CoSe_2$ Heterointerfaces Coupled with Surface High-Valence Bimetallic Sites for Synergistically Enhanced Oxygen Electrocatalysis. Adv Mater 2020;32:2000607. https://doi.org/10.1002/adma.202000607.
[34] Peng X, Xie S, Xiong SJ, Li R, Wang P, Zhang XM, et al. Ultralow-voltage hydrogen production and simultaneous Rhodamine B beneficiation in neutral wastewater. J Energy Chem 2023;81:574–82. https://doi.org/10.1016/j.jechem.2023.03.022.
[35] Zhu YJ, Liu C, Cui SW, Lu ZR, Ye JY, Wen YZ, et al. Multistep Dissolution of Lamellar Crystals Generates Superthin Amorphous $Ni(OH)_2$ Catalyst for UOR. Adv Mater 2023;35:2301549. https://doi.org/10.1002/adma.202301549.
[36] Abdel-Dayem HM. Dynamic phenomena during reduction of α-$NiMoO_4$ in different atmospheres: in-situ thermo-Raman spectroscopy study. Ind Eng Chem Res 2007;46:2466–72. https://doi.org/10.1021/ie0613467.
[37] Zhao X, Cai W, Yang Y, Song XP, Neale Z, Wang H-E, et al. $MoSe_2$ nanosheets perpendicularly grown on graphene with Mo-C bonding for sodium-ion capacitors. Nano Energy 2018;47:224–34. https://doi.org/10.1016/j.nanoen.2018.03.002.
[38] Xu P, Zhang J, Ye Z, Liu Y, Cen T, Yuan D, et al. Co doped $Ni_{0.85}Se$ nanoparticles on RGO as efficient electrocatalysts for hydrogen evolution reaction. Appl Surf Sci 2019;494:749–55. https://doi.org/10.1016/j.apsusc.2019.07.231.
[39] Ran ZQ, Shu CZ, Hou ZQ, Cao LJ, Liang RX, Li JB, et al. Ni_3Se_2/$NiSe_2$ heterostructure nanoforests as an efficient bifunctional electrocatalyst for high-capacity and long-life Li-O_2 batteries. J Power Sources 2020;468:228308. https://doi.org/10.1016/j.jpowsour.2020.228308.
[40] Ou JZ, Campbell JL, Yao D, Wlodarski W, Kalantar-zadeh K. In Situ Raman Spectroscopy of H_2 Gas Interaction with Layered MoO_3. J Phys Chem C 2011;115:10757–63. https://doi.org/10.1021/jp202123a.
[41] Zheng XH, Yang YQ, Sun B, Ning R, Sui JH, Cai W. Lattice Mismatch in Ni_3Se_4-$MoSe_2$ Nanoheterostructures with an Abundant Interface for Catalytic Hydrogen Evolution. ACS Appl Nano Mater 2021;4:3493–9. https://doi.org/10.1021/acsanm.0c03480.
[42] Peng X, Xie S, Wang X, Pi CR, Liu ZT, Gao B, et al. Energy-saving hydrogen production by methanol oxidation reaction coupled hydrogen evolution reaction co-catalyzed by phase separation induced heterostructure. J Mater Chem A 2022;10:20761–9. https://doi.org/10.1039/D2TA02955C.
[43] Peng X, Jin X, Liu NZ, Wang P, Liu ZT, Gao B, et al. A high-performance electrocatalyst composed of nickel clusters encapsulated with a carbon network on TiN nanaowire arrays for the oxygen evolution reaction. Appl Surf Sci 2021;567:150779. https://doi.org/10.1016/j.apsusc.2021.150779.
[44] Bhat KS, Nagaraja HS. Nickel selenide nanostructures as an electrocatalyst for hydrogen evolution reaction. Int J Hydrogen Energ 2018;43:19851–63. https://doi.org/10.1016/j.ijhydene.2018.09.018.
[45] Shi XK, Ling XF, Li LL, Zhong C, Deng YD, Han XP, et al. Nanosheets assembled into nickel sulfide nanospheres with enriched Ni^{3+} active sites for efficient water-splitting and zinc-air batteries. J Mater Chem A 2019;7:23787–93. https://doi.org/10.1039/C9TA03819A.
[46] Peng X, Yan YJ, Xiong SJ, Miao Y, Wen J, Liu ZT, et al. Se-$NiSe_2$ hybrid nanosheet arrays with self-regulated elemental Se for efficient alkaline water splitting. J Mater Sci Technol 2022;118:136–43. https://doi.org/10.1016/j.jmst.2021.12.022.
[47] Yuan FH, Mohammadi MR, Ma LL, Cui Zhu SL, Li ZY, et al ZD. Electrodeposition of self-supported NiMo amorphous coating as an efficient and stable catalyst for hydrogen evolution reaction. Rare Metals 2022;41:2624–32. https://doi.org/10.1007/s12598-022-01967-6.
[48] Zhai PL, Zhang YX, Wu YZ, Gao JF, Zhang B, Cao YS, et al. Engineering active sites on hierarchical transition bimetal oxides/sulfides heterostructure array enabling robust overall water splitting. Nat Commun 2020;11:5462. https://doi.org/10.1038/s41467-020-19214-w.
[49] Wu PY, Sun GY, Chen YZ, Xu WJ, Zheng HF, Xu J, et al. $MoSe_2$-Ni_3Se_4 Hybrid Nanoelectrocatalysts and Their Enhanced Electrocatalytic Activity for Hydrogen Evolution Reaction. Nanoscale Res Lett 2020;15:132. https://doi.org/10.1186/s11671-020-03368-z.
[50] Ma Y, Wang L, Ma JZ, Wang HH, Zhang CB, Deng H, et al. Investigation into the Enhanced Catalytic Oxidation of o-Xylene over MOF-Derived Co_3O_4 with Different Shapes: The Role of Surface Twofold-Coordinate Lattice Oxygen (O_{2f}). ACS Catal 2021;11:6614–25. https://doi.org/10.1021/acscatal.1c01116.
[51] Zhai YY, Ren XR, Sun Y, Li D, Wang B, Liu SZ. Synergistic effect of multiple vacancies to induce lattice oxygen redox in NiFe-layered double hydroxide OER catalysts. Appl Catal B-Environ 2023;323:122091. https://doi.org/10.1016/j.apcatb.2022.122091.
[52] Wang XL, Gong YJ, Shi G, Chow WL, Keyshar K, Ye GL, et al. Chemical Vapor Deposition Growth of Crystalline Monolayer $MoSe_2$. ACS Nano 2014;8:5125–31. https://doi.org/10.1021/nn501175k.
[53] Liu PF, Zhang L, Zheng LR, Yang HG. Surface engineering of nickel selenide for an enhanced intrinsic overall water splitting ability. Mater Chem Front 2018;2:1725–31. https://doi.org/10.1039/C8QM00292D.
[54] Das D, Santra S, Nanda KK. In situ fabrication of a nickel/molybdenum carbide-anchored N-doped graphene/CNT hybrid: an efficient (pre) catalyst for OER and HER. ACS Appl Mater Interfaces 2018;10:35025–38. https://doi.org/10.1021/acsami.8b09941.
[55] Tang GW, Qian Q, Peng KL, Wen X, Zhou GX, et al. Selenium semiconductor core optical fibers. AIP Adv 2015;5:027113. https://doi.org/10.1063/1.4908020.
[56] Si JC, Chen HL, Lei CT, Suo YG, Yang B, Zhang ZG, et al. Electrochemical exfoliation of ultrathin ternary molybdenum sulfoselenide nanosheets to boost the energy-efficient hydrogen evolution reaction. Nanoscale 2019;11:16200–7. https://doi.org/10.1039/C9NR04587B.
[57] Zhang X, Xu HM, Li XX, Li YY, Yang TB, Liang YY. Facile Synthesis of Nickel-Iron/Nanocarbon Hybrids as Advanced Electrocatalysts for Efficient Water Splitting. ACS Catal 2016;6:580–8. https://doi.org/10.1021/acscatal.5b02291.
[58] Kuang P, Tong T, Fan K, Yu J. In situ fabrication of Ni-Mo bimetal sulfide hybrid as an efficient electrocatalyst for hydrogen evolution over a wide pH range. ACS Catal 2017;7:6179–87. https://doi.org/10.1021/acscatal.7b02225.
[59] Zhu ZJ, Yin HJ, He C-T, Al-Mamun M, Liu P-R, Jiang LX, et al. Ultrathin transition metal dichalcogenide/*3d* metal hydroxide hybridized nanosheets to enhance hydrogen evolution activity. Adv Mater 2018;30(28). https://doi.org/10.1002/adma.201801171.
[60] Attanayake NH, Dheer L, Thenuwara AC, Abeyweera SC, Collins C, Waghmare UV, et al. Ni-and Co-substituted metallic MoS_2 for the alkaline hydrogen evolution reaction. ChemElectroChem 2020;7:3606–15. https://doi.org/10.1002/celc.202000532.
[61] Ma FH, Liang Y, Zhou P, Tong FX, Wang ZY, Wang P, et al. One-step synthesis of Co-doped 1T-MoS_2 nanosheets with efficient and stable HER activity in alkaline solutions. Mater Chem Phys 2020;244:122642. https://doi.org/10.1016/j.matchemphys.2020.122642.
[62] Zhao XZ, Liu KK, Guo FB, He ZY, Zhang LX, Lei SW, et al. meta-Position synergistic effect induced by Ni-Mo co-doped WSe_2 to enhance the hydrogen evolution reaction. Dalton Trans 2022;51:11758–67. https://doi.org/10.1039/d2dt01350a.
[63] Guo F-b, Zhao X-y, Yu Y-m, Cheng J, Liu K-k, Zhang L-x. NiMOF-derived $MoSe_2$@$NiSe_2$ heterostructure with hollow core-shell for efficient hydrogen evolution reaction. J Alloys Compd 2023;947:169513–21. https://doi.org/10.1016/j.jallcom.2023.169513.
[64] Guo F-b, Zhao X-y, Lei H-y, Xu Y, Liu K-k, Zhang L-x, et al. Bimetallic doping-derived heterostructures in NiCo-WSe_2 to promote hydrogen evolution reaction. J Alloys Compd 2022;924:166538. https://doi.org/10.1016/j.jallcom.2022.166538.
[65] Feng WS, Bu MM, Kan ST, Gao XH, Guo AM, Liu HT, et al. Interfacial hetero-phase construction in nickel/molybdenum selenide hybrids to promote the water splitting performance. Appl Mater Today 2021;25:101175. https://doi.org/10.1016/j.apmt.2021.101175.
[66] Zhang S, Zhang X, Li J, Wang E. Morphological and Electronic Modulation of NiSe Nanosheet Assemblies by Mo, S-codoping for Efficient Hydrogen Evolution Reaction. J Mater Chem A 2017;5:20588–93. https://doi.org/10.1039/C7TA05991D.

Supporting information

Synergistic Dual-Regulating the Electronic Structure of NiMo Selenides Composite for Highly Efficient Hydrogen Evolution Reaction

Rong Li[1#], Song Xie[1#], Yujie Zeng[1], Qiangqiang Zhao[1], Minqin Mao[1], Zhitian Liu[1], Paul K. Chu[2], Xiang Peng[1]*

[1] Hubei Key Laboratory of Plasma Chemistry and Advanced Materials, Engineering Research Center of Phosphorus Resources Development and Utilization of Ministry of Education, School of Materials Science and Engineering, Wuhan Institute of Technology, Wuhan 430205, China

[2] Department of Physics, Department of Materials Science and Engineering, and Department of Biomedical Engineering, City University of Hong Kong, Tat Chee Avenue, Kowloon, Hong Kong, China

[#] These authors contributed equally to this work.

*Correspondence: xpeng@wit.edu.cn (X. Peng)

Supplementary note I: TOF calculation

TOF values are calculated according to the method reported by the Jaramillo group [1].

The detailed calculation is shown as follows:

To calculate the per-site TOF, we use the following formula:

$$TOF = \frac{number\ of\ total\ hydrogen\ turnovers/cm^2}{number\ of\ active\ of\ sites/cm^2}$$

The total number of hydrogen turnovers is calculated from the current density:

$$No.of\ H_2$$

$$= \left(j\frac{mA}{cm^2}\right)\left(\frac{1\ C\ s^{-1}}{1000\ mA}\right)\left(\frac{1\ mol\ e^{-1}}{96485.3\ C}\right)\left(\frac{1\ mol\ H_2}{2\ mol\ e^{-1}}\right)\left(\frac{6.022\times10^{23}H_2\ mulecules}{1\ mol\ H_2}\right)$$

$$= 3.12\times10^{15}\frac{H_2\ s^{-1}}{cm^2}per\frac{mA}{cm^2}$$

The active sites per real surface area are calculated from the following formula:

$$No.of\ active\ sites = \left(\frac{No.of\ atoms/unit\ cell}{Volunme/unit\ cell}\right)^{\frac{2}{3}}$$

The calculation of the number of active sites of NMS-x should follow the formula:

$$No.of\ active\ sites \times ECSA$$

$$= \left(\frac{No.of\ atoms/unit\ cell}{Volume/unit\ cell}\right)^{\frac{2}{3}} \times x \times ECSA$$

$$+ \left(\frac{No.of\ atoms/unit\ cell}{Volume/unit\ cell}\right)^{\frac{2}{3}} \times y \times ECSA$$

For $MoSe_2$:

$$No.of\ active\ sites = \left(\frac{No.of\ atoms/unit\ cell}{Volunme/unit\ cell}\right)^{\frac{2}{3}}$$

$$No.of\ active\ sites = \left(\frac{3\ atoms/unit\ cell}{120.94\ Å^3/unit\ cell}\right)^{\frac{2}{3}}$$

No. of active sites = 8.5×10^{14} atoms cm^{-2}

$$ECSA = \frac{Specific\ capacitance\ (\mu F\ cm^{-2})}{40\ \mu F\ cm^{-2}\ per\ cm^2_{ECSA}} = A_{geo} \times \frac{3000\ (\mu F\ cm^{-2})}{40\ \mu F\ cm^{-2}}$$

$$TOF = \frac{\left(3.12 \times 10^{15}\ \frac{H_2\ s^{-1}}{cm^2}\ per\ \frac{mA}{cm^2}\right) \times |j|}{no.of\ active\ sites\ \times ECSA}$$

For NMS-1:

$$No.of\ active\ sites = \left(\frac{No.of\ atoms/unit\ cell}{Volunme/unit\ cell}\right)^{\frac{2}{3}}$$

$$No.of\ active\ sites\ (MoSe_2) = \left(\frac{3\ atoms/unit\ cell}{120.94\ Å^3/unit\ cell}\right)^{\frac{2}{3}}$$

No. of active sites ($MoSe_2$) = 8.5×10^{14} atoms cm^{-2}

$$No.of\ active\ sites\ (Ni_{0.85}Se) = \left(\frac{37\ atoms/unit\ cell}{60.14 \times 20\ Å^3/unit\ cell}\right)^{\frac{2}{3}}$$

No. of active sites ($Ni_{0.85}Se$) = 9.8×10^{14}atoms cm^{-2}

$$ECSA = \frac{Specific\ capacitance\ (\mu F\ cm^{-2})}{40\ \mu F\ cm^{-2}\ per\ cm^2_{ECSA}} = A_{geo} \times \frac{31500\ (\mu F\ cm^{-2})}{40\ \mu F\ cm^{-2}}$$

$$TOF$$

$$= \frac{\left(3.12 \times 10^{15}\ \frac{H_2\ s^{-1}}{cm^2}\ per\ \frac{mA}{cm^2}\right) \times |j|}{no.of\ active\ sites\ (MoSe_2) \times x \times ECSA + no.of\ active\ sites\ (Ni_{0.85}Se) \times y \times ECSA}$$

Where x = 50% and y = 50%.

For NMS-2:

$$No.of\ active\ sites = \left(\frac{No.of\ atoms/unit\ cell}{Volumme/unit\ cell}\right)^{\frac{2}{3}}$$

$$No.of\ active\ sites\ (\mathrm{MoSe_2}) = \left(\frac{3\ atoms/unit\ cell}{120.94\ \text{Å}^3/unit\ cell}\right)^{\frac{2}{3}}$$

No. of active sites ($MoSe_2$) = 8.5 ×10^{14} atoms cm^{-2}

$$No.of\ active\ sites\ (\mathrm{Ni_{0.85}Se}) = \left(\frac{37\ atoms/unit\ cell}{60.14 \times 20\ \text{Å}^3/unit\ cell}\right)^{\frac{2}{3}}$$

No. of active sites ($Ni_{0.85}Se$) = 9.8 × 10^{14}atoms cm^{-2}

$$ECSA = \frac{Specific\ capacitance\ (\mu F\ cm^{-2})}{40\ \mu F\ cm^{-2}\ per\ cm^2_{ECSA}} = A_{geo} \times \frac{40250\ (\mu F\ cm^{-2})}{40\ \mu F\ cm^{-2}}$$

$$TOF$$

$$= \frac{\left(3.12 \times 10^{15}\ \frac{H_2\ s^{-1}}{cm^2} per\ \frac{mA}{cm^2}\right) \times |j|}{no.of\ active\ sites\ (MoSe_2) \times x \times ECSA + no.of\ active\ sites\ (\mathrm{Ni_{0.85}Se}) \times y \times ECSA}$$

Where x = 50% and y = 50%.

For NMS-3:

$$No.of\ active\ sites = \left(\frac{No.of\ atoms/unit\ cell}{Volumme/unit\ cell}\right)^{\frac{2}{3}}$$

$$No.of\ active\ sites\ (\mathrm{MoSe_2}) = \left(\frac{3\ atoms/unit\ cell}{120.94\ \text{Å}^3/unit\ cell}\right)^{\frac{2}{3}}$$

No. of active sites ($MoSe_2$) = 8.5 ×10^{14} atoms cm^{-2}

$$No.of\ active\ sites\ (\mathrm{Ni_{0.85}Se}) = \left(\frac{37\ atoms/unit\ cell}{60.14 \times 20\ \text{Å}^3/unit\ cell}\right)^{\frac{2}{3}}$$

No. of active sites ($Ni_{0.85}Se$) = 9.8 × 10^{14}atoms cm^{-2}

$$ECSA = \frac{Specific\ capacitance\ (\mu F\ cm^{-2})}{40\ \mu F\ cm^{-2}\ per\ cm^2_{ECSA}} = A_{geo} \times \frac{577500\ (\mu F\ cm^{-2})}{40\ \mu F\ cm^{-2}}$$

$$TOF = \frac{\left(3.12 \times 10^{15}\ \frac{H_2\ s^{-1}}{cm^2}\ per\ \frac{mA}{cm^2}\right) \times |j|}{no.\ of\ active\ sites\ (MoSe_2) \times x \times ECSA + no.\ of\ active\ sites\ (Ni_{0.85}Se) \times y \times ECSA}$$

Where x = 50% and y = 50%.

For NMS-4:

$$No.\ of\ active\ sites = \left(\frac{No.\ of\ atoms/unit\ cell}{Volumme/unit\ cell}\right)^{\frac{2}{3}}$$

$$No.\ of\ active\ sites\ (MoSe_2) = \left(\frac{3\ atoms/unit\ cell}{120.94\ Å^3/unit\ cell}\right)^{\frac{2}{3}}$$

No. of active sites ($MoSe_2$) = 8.5×10^{14} atoms cm^{-2}

$$No.\ of\ active\ sites\ (Ni_{0.85}Se) = \left(\frac{37\ atoms/unit\ cell}{60.14 \times 20\ Å^3/unit\ cell}\right)^{\frac{2}{3}}$$

No. of active sites ($Ni_{0.85}Se$) = 9.8×10^{14}atoms cm^{-2}

$$ECSA = \frac{Specific\ capacitance\ (\mu F\ cm^{-2})}{40\ \mu F\ cm^{-2}\ per\ cm^2_{ECSA}} = A_{geo} \times \frac{122500\ (\mu F\ cm^{-2})}{40\ \mu F\ cm^{-2}}$$

$$TOF = \frac{\left(3.12 \times 10^{15}\ \frac{H_2\ s^{-1}}{cm^2}\ per\ \frac{mA}{cm^2}\right) \times |j|}{no.\ of\ active\ sites\ (MoSe_2) \times x \times ECSA + no.\ of\ active\ sites\ (Ni_{0.85}Se) \times y \times ECSA}$$

Where x = 50% and y = 50%.

For $Ni_{0.85}Se$:

$$No.of\ active\ sites = \left(\frac{No.of\ atoms/unit\ cell}{Volumme/unit\ cell}\right)^{\frac{2}{3}}$$

$$No.of\ active\ sites\ (\mathrm{Ni_{0.85}Se}) = \left(\frac{37\ atoms/unit\ cell}{60.14 \times 20\ \text{Å}^3/unit\ cell}\right)^{\frac{2}{3}}$$

No. of active sites = 8.5×10^{14} atoms cm^{-2}

$$ECSA = \frac{Specific\ capacitance\ (\mu F\ cm^{-2})}{40\ \mu F\ cm^{-2}\ per\ cm^2_{ECSA}} = A_{geo} \times \frac{1000\ (\mu F\ cm^{-2})}{40\ \mu F\ cm^{-2}}$$

$$TOF = \frac{\left(3.12 \times 10^{15}\ \frac{H_2\ s^{-1}}{cm^2}\ per\ \frac{mA}{cm^2}\right) \times |j|}{no.of\ active\ sites\ \times ECSA}$$

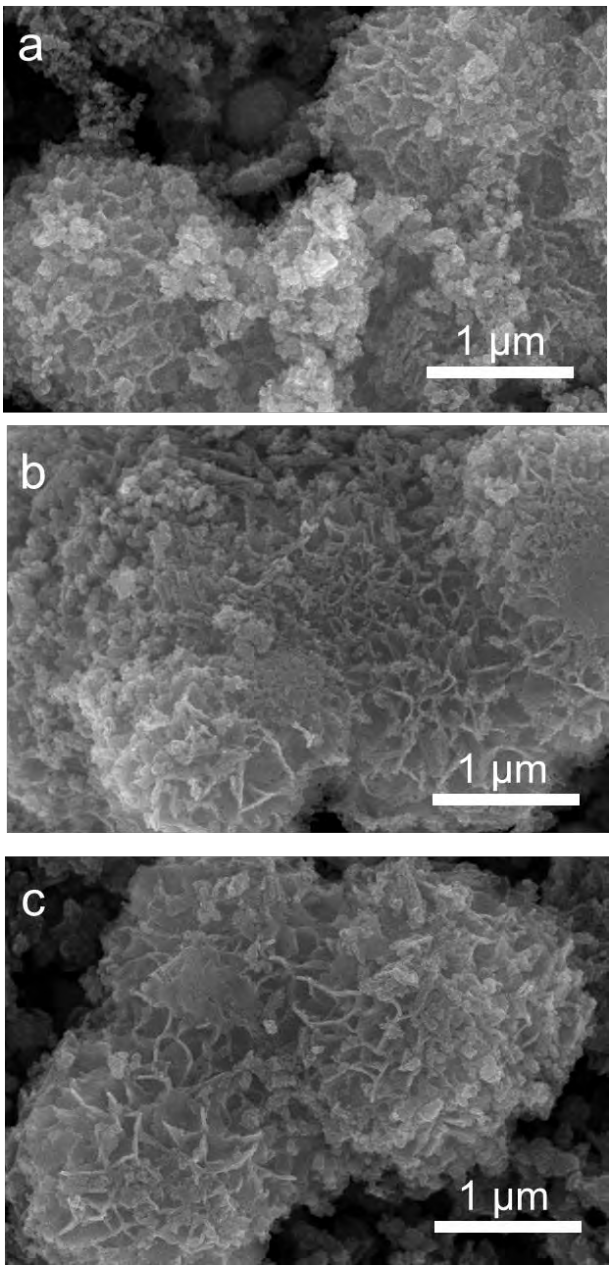

Figure S1. SEM images: (a) NMS-1, (b) NMS-2, and (c) NMS-4.

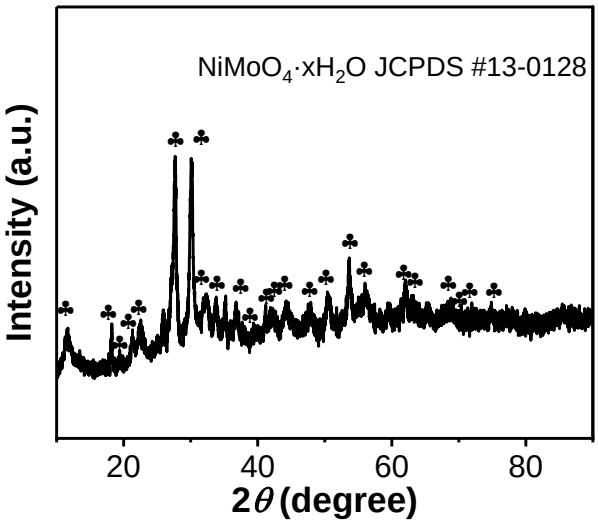

Figure S2. XRD pattern of $NiMoO_4 \cdot xH_2O$.

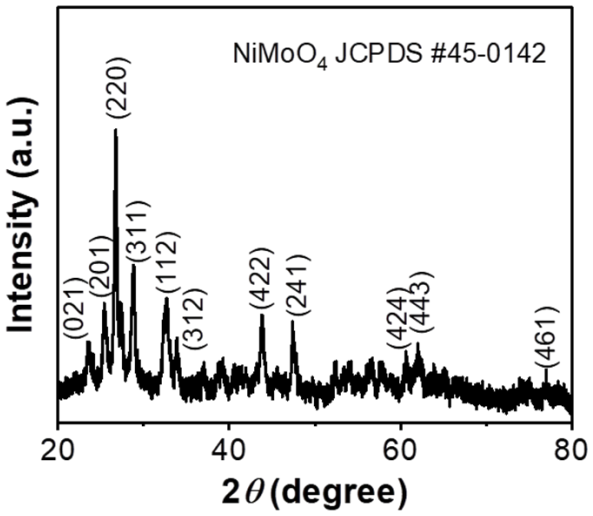

Figure S3. XRD pattern of $NiMoO_4$.

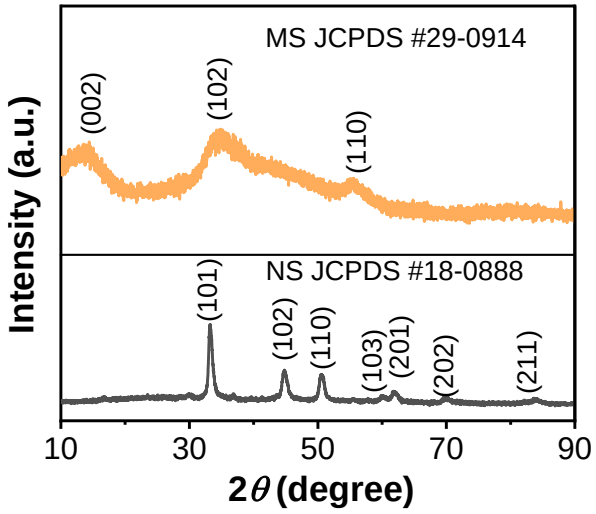

Figure S4. XRD patterns of the pure-phase NS and MS.

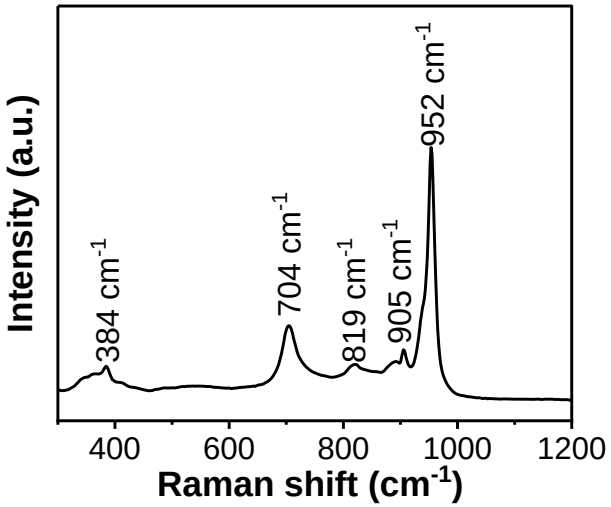

Figure S5. Raman scattering spectrum of $NiMoO_4$.

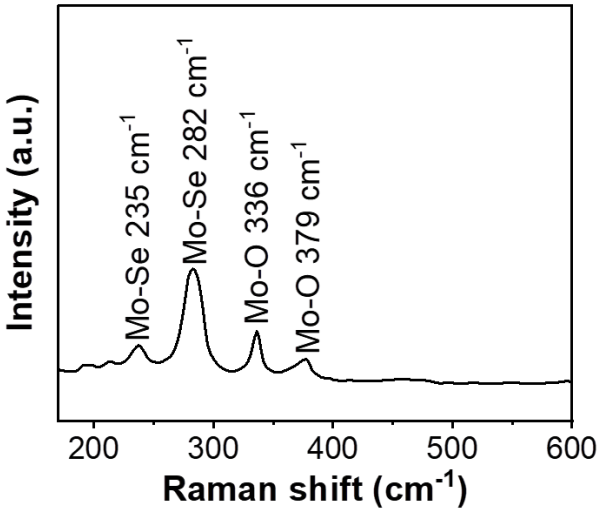

Figure S6. Raman scattering spectrum of MS.

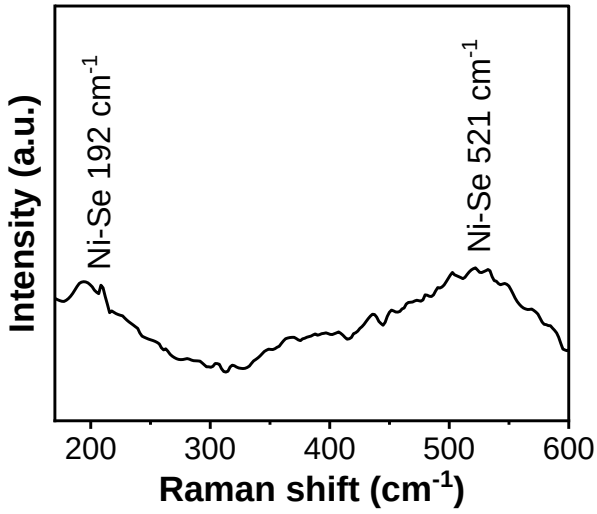

Figure S7. Raman scattering spectrum of NS.

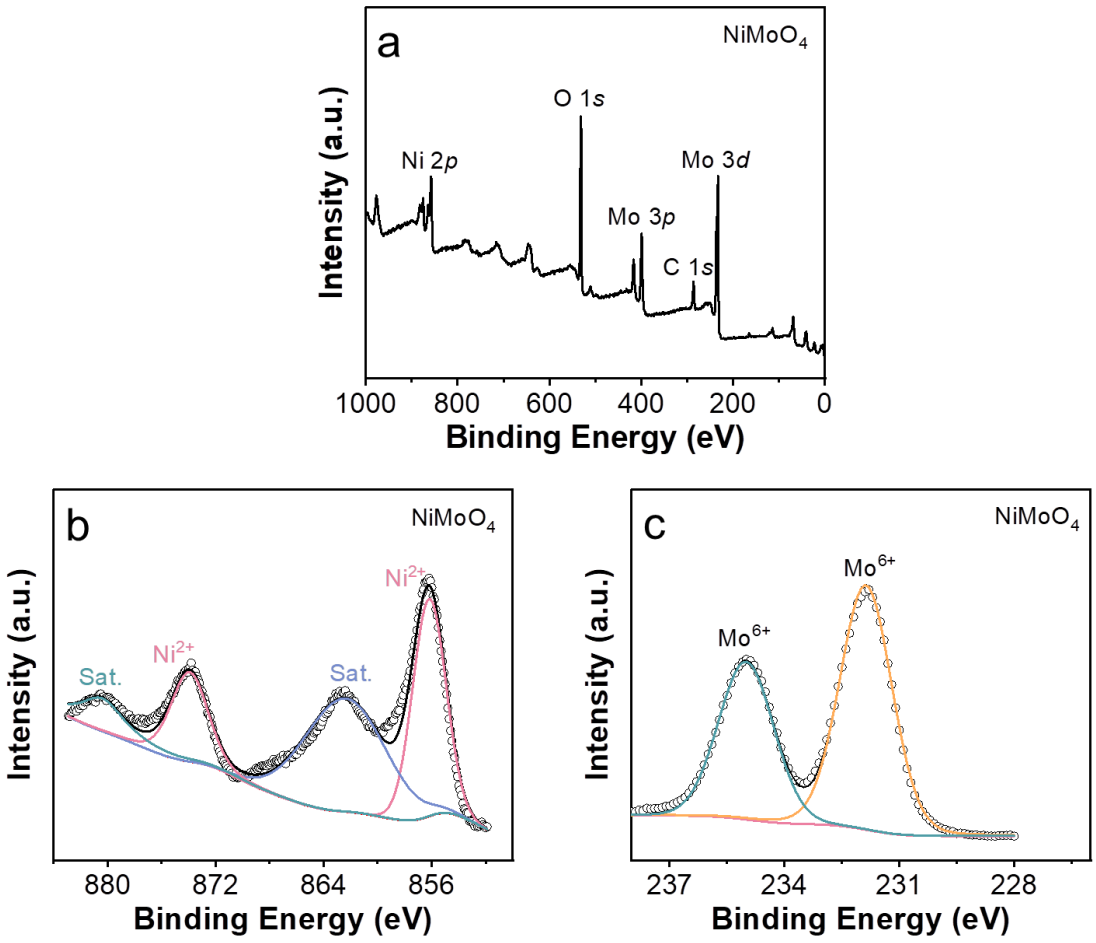

Figure S8. XPS spectra of the $NiMoO_4$: (a) Survey, (b) Ni-2*p*, and (c) Mo-3*d*.

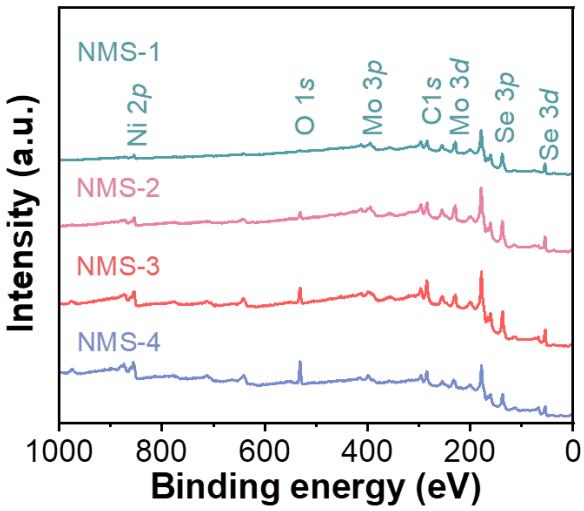

Figure S9. XPS survey spectra of NMS-1, NMS-2, NMS-3, and NMS-4.

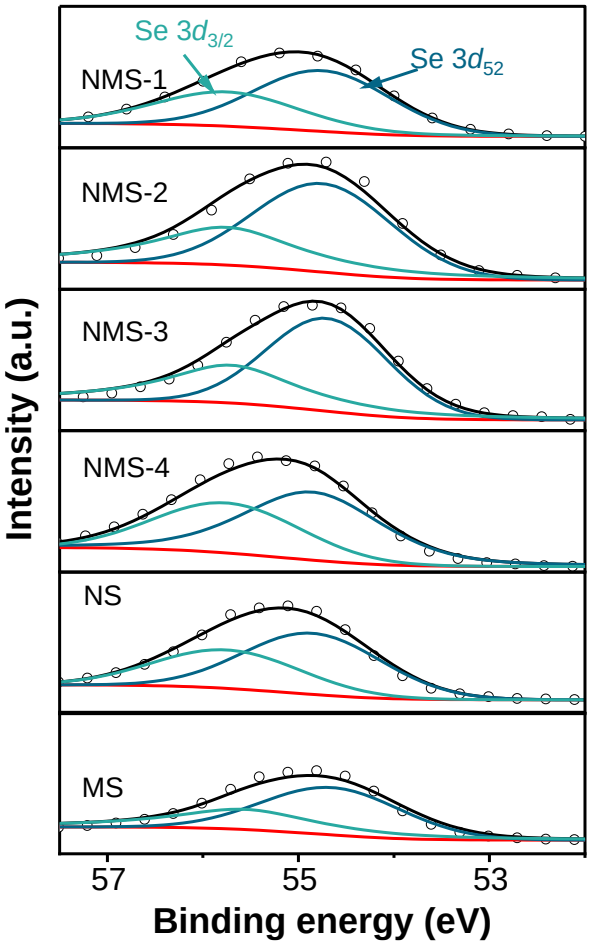

Figure S10. XPS spectra of Se-3*d*.

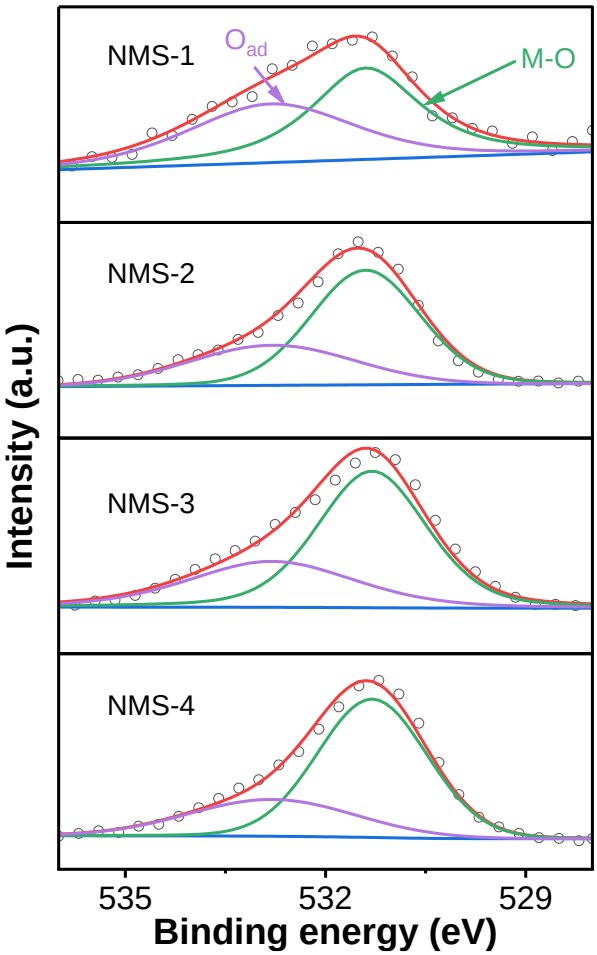

Figure S11. High-resolution XPS O-1*s* spectra of NMS-x.

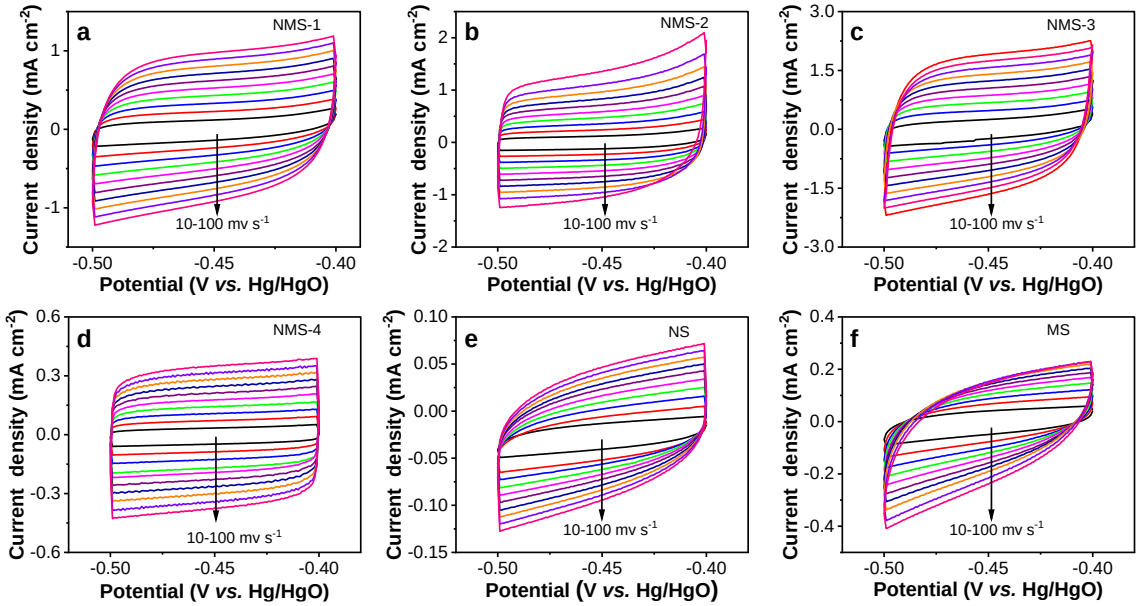

Figure S12. Cyclic voltammetry (CV) curves of (a) NMS-1, (b) NMS-2, (c) NMS-3, (d) NMS-4, (e) NS, and (f) MS acquired at scanning rates between 10 and 100 mV s^{-1}.

Table S1. Comparison of the HER characteristics of different electrocatalysts.

Catalysts	η_{10} (mV)	Tafel slope (mV dec^{-1})	Refs.
Ni/Mo_xC	161	104	[2]
NiS	220	145	[3]
NiS_2	147	105	[3]
EG/$Co_{0.85}Se$/NiFe-LDH	260	160	[4]
$MoSe_xS_{2-x}$	248	123	[5]
$Ni_{0.9}Fe_{0.1}$/NC	231	111	[6]
$Ni_{0.8}Fe_{0.2}$/NC	253	110	[6]
$Ni_{0.7}Fe_{0.3}$/NC	297	119	[6]
$Ni_{0.6}Fe_{0.4}$/NC	337	110	[6]
$NiSe_2$/CC-180	133	128	[7]
NiS_2/MoS_2 HNW	204	65	[8]
2D-$MoS_2/Co(OH)_2$	128	76	[9]
Co/M-MoS_2	165	124	[10]
Co-1T-MoS	240	68	[11]
Ni-Mo co-doped WSe_2	188	122	[12]
NiMOF-$MoSe_2$@$NiSe_2$	187	71	[13]
NiCo-WSe_2	205	118	[14]
NiMoSe/NF-1	91	48	[15]
Mo,S-codoped NiSe/NF	88	82	[16]

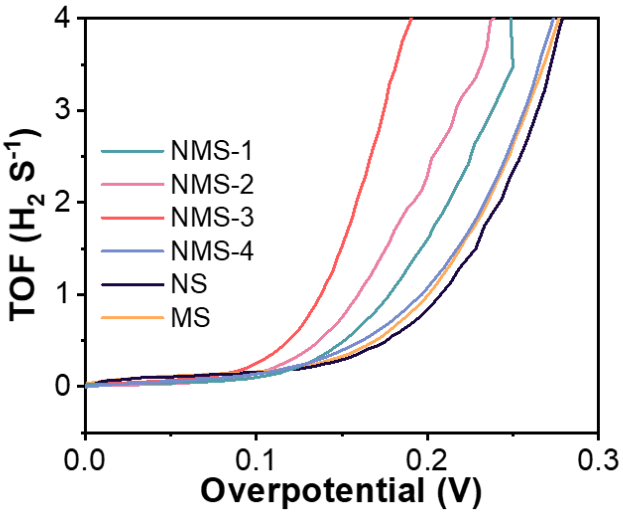

Figure S13. TOF of (1) NMS-1, (2) NMS-2, (3) NMS-3, (4) NMS-4, (5) MS, and (6) NS modified GCE in 1.0 M KOH.

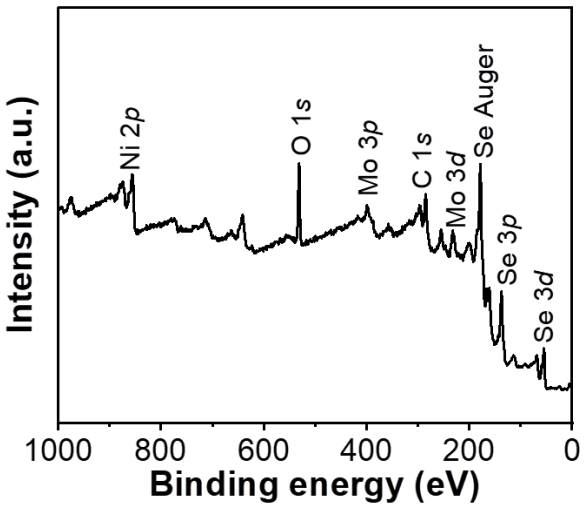

Figure S14. XPS survey spectrum of NMS-3 after the long-term test.

References

[1] Kibsgaard J, Jaramillo TF. Molybdenum Phosphosulfide: An Active, Acid-Stable, Earth Abundant Catalyst for the Hydrogen Evolution Reaction. Angew Chem Int Ed 2014;53:1-6. https://doi.org/10.1002/anie.201408222.

[2] Das D, Santra S, Nanda KK. In situ fabrication of a nickel/molybdenum carbide-anchored N-doped graphene/CNT hybrid: an efficient (pre) catalyst for OER and HER. ACS Appl Mater Interfaces 2018;10:35025-38. https://doi.org/10.1021/acsami.8b09941.

[3] Shi X, Ling X, Li L, Zhong C, Deng Y, Han X, Hu W. Nanosheets assembled into nickel sulfide nanospheres with enriched Ni^{3+} active sites for efficient water-splitting and zinc–air batteries. J Mater Chem A 2019;7:23787-93. https://doi.org/10.1039/C9TA03819A.

[4] Tang G, Qian Q, Peng K, Wen X, Zhou G, Sun M, Chen X, Yang Z. Selenium semiconductor core optical fibers. AIP Adv 2015;5:027113. https://doi.org/10.1063/1.4908020.

[5] Si J, Chen H, Lei C, Suo Y, Yang B, Zhang Z, Li Z, Lei L, Chen J, Hou Y. Electrochemical exfoliation of ultrathin ternary molybdenum sulfoselenide nanosheets to boost the energy-efficient hydrogen evolution reaction. Nanoscale 2019;11:16200-7. https://doi.org/10.1039/C9NR04587B.

[6] Zhang X, Xu H, Li X, Li Y, Yang T, Liang Y. Facile Synthesis of Nickel–Iron/Nanocarbon Hybrids as Advanced Electrocatalysts for Efficient Water Splitting. ACS Catal 2016;6:580-8. https://doi.org/10.1021/acscatal.5b02291.

[7] Peng X, Yan Y, Xiong S, Miao Y, Wen J, Liu Z, Gao B, Hu L, Chu PK. Se-$NiSe_2$ hybrid nanosheet arrays with self-regulated elemental Se for efficient alkaline water

splitting. J Mater Sci Technol 2022;118:136-43. https://doi.org/10.1016/j.jmst.2021.12.022.

[8] Kuang P, Tong T, Fan K, Yu J. In situ fabrication of Ni–Mo bimetal sulfide hybrid as an efficient electrocatalyst for hydrogen evolution over a wide pH range. ACS Catal 2017;7:6179-87. https://doi.org/10.1021/acscatal.7b02225.

[9] Zhu Z, Yin H, He CT, Al‐Mamun M, Liu P, Jiang L, Zhao Y, Wang Y, Yang HG, Tang Z. Ultrathin transition metal dichalcogenide/3*d* metal hydroxide hybridized nanosheets to enhance hydrogen evolution activity. Adv Mater 2018;30:1801171. https://doi.org/10.1002/adma.201801171.

[10] Attanayake NH, Dheer L, Thenuwara AC, Abeyweera SC, Collins C, Waghmare UV, Strongin DR. Ni- and Co-substituted metallic MoS_2 for the alkaline hydrogen evolution reaction. ChemElectroChem 2020;7:3606-15. https://doi.org/10.1002/celc.202000532.

[11] Ma F, Liang Y, Zhou P, Tong F, Wang Z, Wang P, Liu Y, Dai Y, Zheng Z, Huang B. One-step synthesis of Co-doped 1T-MoS_2 nanosheets with efficient and stable HER activity in alkaline solutions. Mater Chem Phys 2020;244:122642. https://doi.org/10.1016/j.matchemphys.2020.122642.

[12] Zhao X, Liu K, Guo F, He Z, Zhang L, Lei S, Li H, Cheng Y, Yang L. meta-Position synergistic effect induced by Ni-Mo co-doped WSe_2 to enhance the hydrogen evolution reaction. Dalton Trans 2022;51:11758-67. https://doi.org/10.1039/d2dt01350a.

[13] Guo F-b, Zhao X-y, Yu Y-m, Cheng J, Liu K-k, Zhang L-x. NiMOF-derived $MoSe_2$@$NiSe_2$ heterostructure with hollow core-shell for efficient hydrogen evolution

reaction. J Alloys Compd 2023;947:169513-21. https://doi.org/10.1016/j.jallcom.2023.169513.

[14] Guo F-b, Zhao X-y, Lei H-y, Xu Y, Liu K-k, Zhang L-x, Xue J-m, Sun H-r. Bimetallic doping-derived heterostructures in NiCo-WSe_2 to promote hydrogen evolution reaction. J Alloys Compd 2022;924:166538. https://doi.org/10.1016/j.jallcom.2022.166538.

[15] Feng W, Bu M, Kan S, Gao X, Guo A, Liu H, Deng L, Chen W. Interfacial hetero-phase construction in nickel/molybdenum selenide hybrids to promote the water splitting performance. Appl Mater Today 2021;25:101175. https://doi.org/10.1016/j.apmt.2021.101175.

[16] Zhang S, Zhang X, Li J, Wang E. Morphological and Electronic Modulation of NiSe Nanosheets Assemblies by Mo, S-codoping for Efficient Hydrogen Evolution Reaction. J Mater Chem A 2017;5:20588-93. https://doi.org/10.1039/C7TA05991D.